Volume 11
Number 30
14 August 2023
Pages 15989–16418

Journal of Materials Chemistry A

Materials for energy and sustainability

rsc.li/materials-a

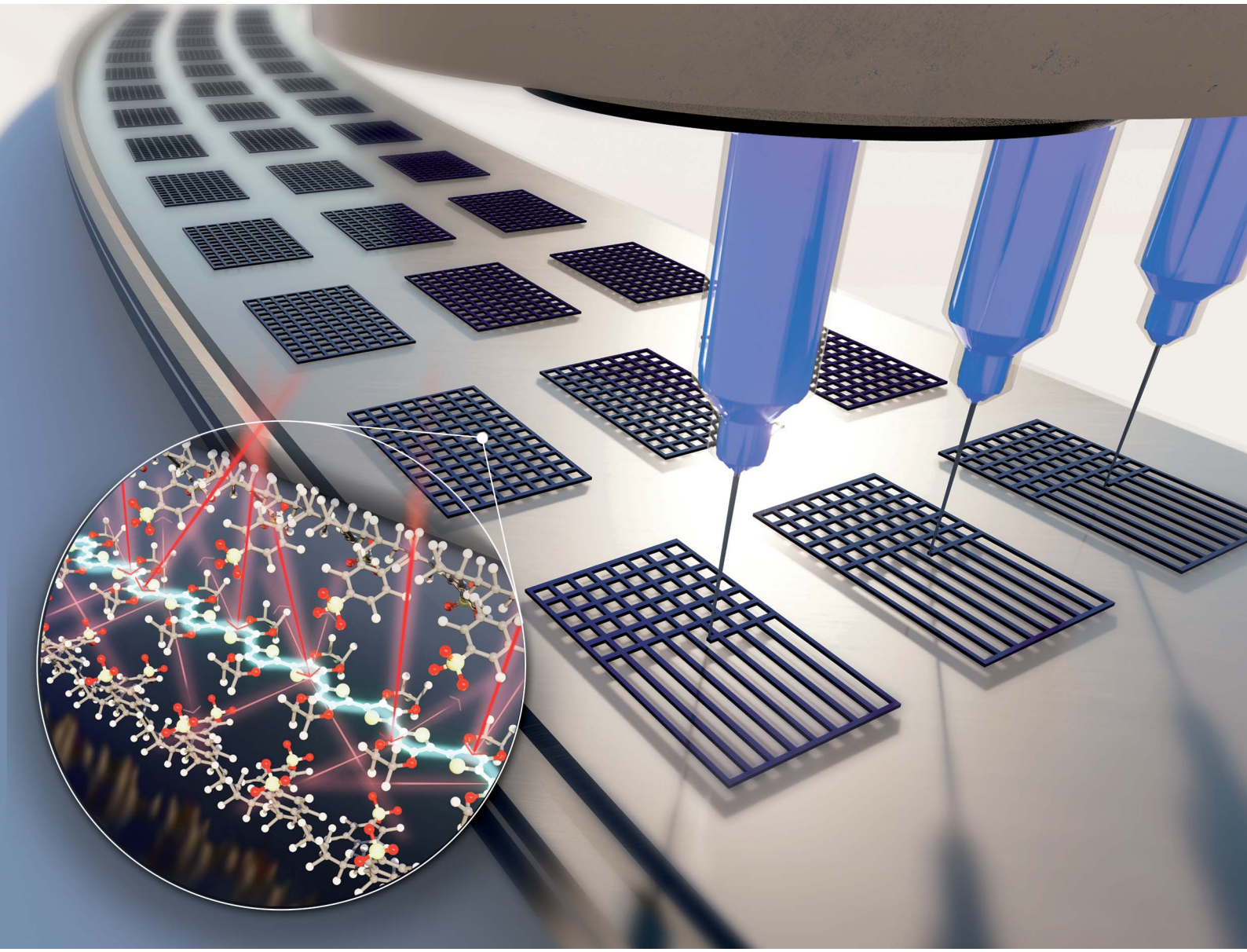

ISSN 2050-7488

ROYAL SOCIETY OF CHEMISTRY

PAPER
Mohammad Arjmand *et al.*
3D printing of solvent-treated PEDOT:PSS inks for electromagnetic interference shielding

10 YEARS ANNIVERSARY

Journal of Materials Chemistry A

ROYAL SOCIETY OF CHEMISTRY

PAPER

View Article Online
View Journal | View Issue

Cite this: J. Mater. Chem. A, 2023, 11, 16027

3D printing of solvent-treated PEDOT:PSS inks for electromagnetic interference shielding†

Saeed Ghaderi, [a] Hadi Hosseini,[a] Seyyed Arash Haddadi, [a] Milad Kamkar [b] and Mohammad Arjmand *[a]

Received 18th February 2023
Accepted 7th June 2023

DOI: 10.1039/d3ta01021j

rsc.li/materials-a

3D printing of conductive polymers has been achieved very recently by direct ink writing of poly(3,4-ethylenedioxythiophene):polystyrene sulfonate (PEDOT:PSS)-based inks. This field is in its infancy, calling for further research to broaden the application horizon of 3D-printed conductive polymers by fine-tuning their inherent properties. Indeed, engineering PEDOT:PSS inks with customizable electrical properties while keeping their rheological fingerprint within the proper range for high-fidelity 3D printing is an arduous challenge, yet to be achieved. Herein, a range of PEDOT:PSS-based inks are formulated by molecular engineering *via* co-solvent doping and solvent post-treatment with various solvents for high-resolution (line width and thickness variations less than 20% from average values), high-aspect-ratio (≥25 layers) 3D printing. *Via* a simple dry-annealing technique, rationally patterned flexible, self-standing, and geometry-friendly samples featuring a wide range of conductivity, *i.e.*, from 0.6 to 858.1 ± 60.8 S cm^{-1}, are fabricated. The results showed that the 3D-printed samples are wet-transferable onto uneven substrates and complex objects with sharp edges. By exploiting their tunable molecular-scale chemistry and macro-scale geometrical features, the 3D-printed devices were used to create advanced electromagnetic shields with controlled mechanisms.

[a]Nanomaterials and Polymer Nanocomposites Laboratory (NPNL), School of Engineering, University of British Columbia, Kelowna, BC, V1V 1V7, Canada. E-mail: mohammad.arjmand@ubc.ca

[b]Department of Chemical Engineering, Waterloo Institute for Nanotechnology, University of Waterloo, 200 University Avenue West, Waterloo, ON, N2L 3G1, Canada

† Electronic supplementary information (ESI) available. See DOI: https://doi.org/10.1039/d3ta01021j

Dr Mohammad Arjmand is a leading and award-winning researcher in the areas of nanotechnology and polymer science and engineering. Dr Arjmand is a faculty member (since 2018) at the University of British Columbia, Okanagan campus (UBCO). He is also a Canada Research Chair in Advanced Materials and Polymer Engineering and the technical lead of the Plastic Recycling Research Cluster at UBCO. Dr Arjmand directs the Nanomaterials and Polymer Nanocomposites Laboratory (NPNL), which focuses on the synthesis and engineering of multifunctional nanomaterials and polymer nanocomposites. Prior to joining UBCO, Dr Arjmand was a postdoctoral fellow at the Universities of Calgary and Toronto.

1. Introduction

As a newly emerged electrically conductive polymer, poly(3,4-ethylenedioxythiophene):polystyrene sulfonate (PEDOT:PSS), has opened a new chapter in the history of organic electronics.[1] PEDOT:PSS has been used to fabricate a wide range of electronic devices, such as flexible electronics,[2] soft actuators,[3] optoelectronics and storage devices,[4] thermoelectric devices,[5] supercapacitors,[6] solar cells,[7] transparent electrodes,[8] electromagnetic interference (EMI) shields,[9] and sensors.[10] Organic electronics based on PEDOT:PSS benefit from water processability, tunable electrical conductivity, chemical and electrical stability, superior flexibility, and lightweight.[1,2]

PEDOT is a low band gap conductive polymer, which has a stable and bipolaronic conductive state.[11,12] Short PEDOT oligomers (~6–18 repeating units) are π-stacked, forming a highly crystalline state that provides high electrical conductivity.[13,14] When PEDOT is doped with PSS through oxidative polymerization, a stable dispersion of PEDOT:PSS in water can be formed, consisting of conductive PEDOT-rich cores and non-conductive PSS-rich shells.[12,15] PSS plays the role of charge-balancing counterion for PEDOT cations and renders them water processable, in the form of micron-sized gel particles.[11] However, the existence of insulating PSS-rich domains is detrimental to the electrical conductivity of PEDOT-based products.

It has been shown that the addition of polar or high-dielectric co-solvents as secondary dopants and/or post-treatment agents significantly modifies the electrical conductivity of PEDOT:PSS systems.[16] In this regard, PSS is considered the primary dopant for PEDOT, and the doping agents are referred to as secondary dopants. To date, the conductivity enhancement of PEDOT:PSS in the presence of solvents has been attributed to different factors, including change in PEDOT grains size[17–19] and crystallinity,[20,21] Coulombic screening effect between PEDOT and PSS[22] along with the phase separation between PEDOT-rich grains and PSS-rich segments. These lead to the partial removal of the non-conductive PSS segments from the conductive PEDOT-rich cores and, thus, turn the coil conformation into an extended linear structure.[1,23–25] However, there is no consensus among scientists on the main mechanisms responsible for the conductivity enhancement of solvent-treated PEDOT:PSS structures.

Another challenge with regard to the widespread utilization of highly conductive PEDOT-based products is the lack of precise control over PEDOT:PSS aqueous systems processing. In common manufacturing techniques such as spin coating,[26] screen printing,[27,28] ink-jet printing,[29,30] electrochemical patterning,[31] and aerosol printing,[32] high costs, long processing time, limitations in production of complex geometries, and low-quality end products negatively affect actual benefits.[33] As an innovative alternative, direct ink writing (DIW) offers a material-saving technique for printing inks with desirable rheological properties onto various substrates. This technique allows for unparalleled flexibility in customization, intricate geometry design, and the creation of miniaturized patterned structures.[34,35]

Indeed, rheological parameters are the cornerstone of a successful DIW process, controlling the flowability of the inks during and after printing to form self-supporting layers.[36–38] Intense shear-thinning behavior conjugated with high yield stress bestows inks with fluid-like behavior during printing and a solid-like behavior immediately after printing.[37,39] Recently, it has been shown that inks containing 7 wt% PEDOT:PSS possess proper rheological properties for high fidelity 3D printing of implantable conductive patches.[33] Further to that, it was shown that the addition of 2D MXenes nanosheets to PEDOT:PSS inks contributes to improving their rheological properties, leading to high-resolution printed lines.[40]

Despite the extensive number of studies, the literature lacks a comprehensive study on the rheological response, printability, and topographical properties of 3D-printed pure PEDOT:PSS-based devices. Hereby, for the first time, we reported a range of pure PEDOT:PSS inks with significantly enhanced electrical conductivity and fine-tuned rheological features for the fabrication of 3D-printed electronics and electromagnetic interference (EMI) shields. This was achieved by molecular engineering *via* co-solvent doping or solvent post-treatment with various solvents. Experimental analyses enabled us to expound on the mechanisms of electrical conductivity enhancement of PEDOT:PSS inks in the presence of various low and high boiling point solvents, including DMSO, EG, DMF, MeOH, and EtOH. Digital, laser microscopy, and scanning electron microscopy (SEM) images were employed to assess the morphology and the printing quality of the printed structures based on the devised inks. In the last step, the effects of the co-solvent type, number of printed layers, infill density, and drying technique on the EMI performance of the 3D printed structures were explored over 8.2 to 12.4 GHz.

2. Materials and methods

2.1. Raw materials

PEDOT:PSS (1 : 2.5) (Clevios PH1000, Heraeus) aqueous dispersion (1–1.3 wt%) was ultrasonicated for 10 min followed by filtration with a 0.45 μm syringe filter (Sterlitech) to remove agglomerations. Organic solvents, including dimethyl sulfoxide (DMSO), ethylene glycol (EG), dimethylformamide (DMF), methanol (MeOH), and ethanol (EtOH) (Sigma Aldrich, ≥99.5%), were used for co-solvent doping and solvent post-treatment. Polydimethylsiloxane (PDMS) (Sylgard 184) was purchased from Dow Corning Corporation, Midland, MI, USA.

2.2. Experimental

2.2.1. Co-solvent doping and solvent post-treatment. To prepare PEDOT:PSS inks, first, the filtered PEDOT:PSS aqueous dispersion was frozen at −85 °C for 24 h and then dried using a freeze-dryer machine for 72 h. Then, different concentrations of the resulting isolated foam-like PEDOT:PSS nanofibrils were re-dispersed in deionized water without and with co-solvents (DMSO, EG, and DMF) at different concentrations, followed by stirring for 12 h (1000 rpm, 25 °C). The final homogenized dispersions of PEDOT:PSS inks were kept at 4 °C for further characterization and printing. The resulting dispersions without co-solvents (pristine PEDOT:PSS aqueous dispersions) were used for the solvent post-treatment process. To do this, the printed pristine PEDOT:PSS ink was first printed with various patterns and then dry-annealed at 140 °C for 2 h. Next, the dry-annealed samples were fully immersed for 30 min at room temperature in one of the five solvents (DMSO, EG, DMF, MeOH, and EtOH), followed by washing out with deionized water (three times) and then drying in an oven at 140 °C for 2 h. It is worth mentioning that in co-solvent doping, PEDOT:PSS dispersion contained water (as the primary solvent) and one of the DMSO, EG, and DMF solvents (as the co-solvents). However, for solvent post-treatment, the dried pristine PEDOT:PSS was immersed in one of the pure solvents (DMSO, EG, DMF, MeOH, or EtOH) without water.

In the current research, the term "doped/undoped" is used for the case of doping PEDOT with PSS chains. Doped PSS chains are those that have interacted with PEDOT chains and undoped PSS are those that are free in the system. While the term "co-solvent doping" is used when a mixture of water and one of the high-boiling-point solvents (*e.g.*, DMSO, EG, and DMF) is used for enhancing the electrical conductivity of PEDOT:PSS. The term "solvent post-treatment" is used when one of the five pure solvents (*e.g.*, DMSO, EG, DMF, MeOH, and EtOH) was employed to enhance the electrical conductivity of PEDOT:PSS.

2.2.2. 3D printing. Before printing, first, the prepared inks were homogenized with a high-speed homogenizer and then loaded into 10 mL syringes. Then, the syringes were centrifuged (2000 rpm, 5 min) to remove all the bubbles. Finally, the resulting homogeneous inks were printed using an extrusion-based Allevi 2 bioprinter, 2-axis micro-positioning stage (Allevi, Philadelphia, PA, USA) in patterned structures designed by CAD models. The printer was driven by a compressed air system to pressurize the syringe barrel (up to 110 psi) and control the printing flow rate. Different patterns were printed on glass and flexible substrates using printing speed, layer thickness, and nozzle diameter of 6–10 mm s^{-1}, 0.2–0.3 mm, and 280 μm, respectively. To manufacture free-standing PEDOT:PSS structures, the prepared inks were printed on the PDMS thin films followed by dry-annealing treatment and then peeled off from the substrate. The PDMS elastomer (Sylgard 184) and its hardener were mixed (10 : 1) and spin-coated (300 rpm, 30 s) on glass slides followed by curing at 90 °C for 2 h.

2.2.3. Techniques and analyses. All methods of characterization are described in detail in the ESI.†

3. Results and discussion

3.1. Rheology and DIW

PEDOT:PSS dispersion in water establishes a dark-blue dispersion of colloidal polymeric micro-gel particles, consisting of a physically crosslinked conductive PEDOT-rich core encased in a non-conductive PSS-rich shell (see Fig. S1†). The gel particle size of the developed dispersion dramatically affects electrical conductivity and viscosity.[1] The smaller the gel particle size, the lower the conductivity and viscosity.[11] The chemical structure of positively charged PEDOT and negatively charged PSS is shown in Fig. S1a.† By increasing the concentration of the PEDOT:PSS micro-gels, the viscosity of the resulting dispersion changes significantly. Inks based on PEDOT:PSS demonstrate a distinct shear-thinning behavior, and the shear-thinning response is intensified by the addition of co-solvents. By increasing the concentration of PEDOT:PSS from 1 to 8 wt%, the shear viscosity and, thus, the shear stresses increased by three orders of magnitude through the whole range of the applied shear rate (see Fig. S2 and S3†). This increase is a strong function of the gel particle size and, consequently, the formation of particle–particle junctions, floc–floc interactions, and the rise of possible entanglements. Similar to solid materials, in which yield stress is identified as the transition from an elastic to a plastic state, for fluids, yield stress is defined as the minimum stress required to demolish the integrated network throughout the medium and transform the ink from a solid-like form to a liquid-like gel.[41]

Furthermore, strain sweep tests (Fig. S4†) showed that at small shear strain amplitudes (<1%), the inks are in their linear viscoelastic region (LVR). Therefore, 0.1% strain was chosen as a safe shear strain for conducting dynamic rheology analyses. Inks based on PEDOT:PSS present a shear-yielding behavior; that is, by increasing the applied shear stress, the viscoelastic

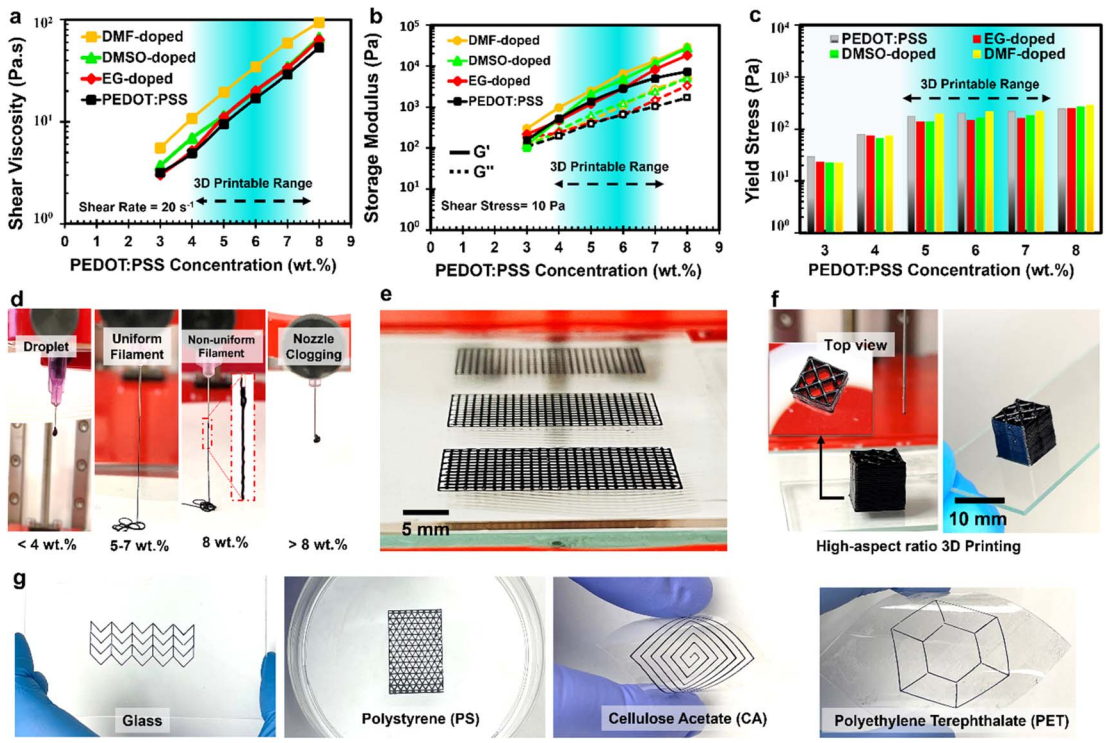

Fig. 1 3D printable range based on shear viscosity (a), storage moduli (b), and yield stress (c) as a function of PEDOT:PSS concentration. Digital images of filament formation at various concentrations of DMSO-doped PEDOT:PSS ink (d). High-resolution one-layer (e) and high-aspect-ratio (f) 3D-printed DMSO-doped PEDOT:PSS ink. Direct ink writing of DMSO-doped PEDOT:PSS ink on glass, polystyrene, cellulose acetate, and polyethylene terephthalate substrates (g). All the printed structures are based on 6 wt% PEDOT:PSS doped with water : DMSO 93 : 7 vol/vol ink.

moduli of the inks drop sharply, indicating the breakage of the gel network upon increasing the shear rate (Fig. S5†). The shear-yielding response is defined by the yield stress value at which the loss modulus (G″) value crosses over the storage modulus (G′) value, meaning that at shear stresses lower than the yield stress, the ink shows a solid-like behavior and can maintain its printed shape.[42,43] Ideally, inks should have appropriate rheological responses after printing. This allows filament formation, prevents the filament from sagging because of its weight, and avoids lateral spreading upon deposition on the printing bed.

The summarized results for shear viscosity and storage and loss moduli coupled with filament formation assessment (Fig. 1a–d) showed that at concentrations lower than 4 wt% of PEDOT:PSS, inks are more likely to form droplets rather than filaments, attributed to low rheological properties. However, in the concentration range of 4–7 wt%, extrusion of a uniform and continuous filament is possible. At concentrations higher than 7 wt%, extrusion of a uniform filament was found to be challenging due to the high shear viscosity and yield stress. Nozzle clogging hinders successful printing at concentrations higher than 8 wt% (Fig. 1d). By taking the rheological properties and extrusion printability into account, the printability region could be defined as a domain of PEDOT:PSS concentration within which a uniform and continuous filament can be extruded from the printing nozzle (refer to the highlighted areas in Fig. 1a–c and ESI Video 1† for 6 wt% PEDOT:PSS doped with water : DMSO 93 : 7 vol/vol ink). Fig. 1a and b exhibit the obtained shear viscosities at a constant shear rate (20 s^{-1}) and the achieved storage and loss moduli values at a constant shear stress of 10 Pa for different PEDOT:PSS-based inks, respectively. Fig. 1c shows the calculated yield stress at shear stresses where the loss modulus (G″) exceeds the storage modulus (G′) curve (see Fig. S5†). DMSO-doped PEDOT:PSS showed the greatest improvement in the electrical conductivity of PEDOT:PSS compared to EG and DMF (refer to the Electrical conductivity measurements section). As such, inks based on 6 wt% PEDOT:PSS doped with water : DMSO 93 : 7 vol/vol (858.1 ± 60.8 S cm^{-1}) were used for further characterization (*e.g.*, printing, structural, mechanical, and EMI shielding evaluations), and are referred to as DMSO-doped PEDOT:PSS in the following. In the case of 6 wt% PEDOT:PSS inks doped with EG and DMF co-solvents, the maximum electrical conductivity of 625.31 ± 39.98 S cm^{-1} (water : EG 95 : 5 vol/vol) and 492.81 ± 42 S cm^{-1} (water : DMF 95 : 5 vol/vol) were achieved, respectively, labeled as EG-doped and DMF-doped PEDOT:PSS in the current research.

By increasing the number of deposited layers, the weight of the deposited layers increases, leading to lateral spreading and, thus, the collapse of the structure. However, proper viscoelastic properties provide shape retention. This combined with higher printing resolution suggests that manufacturing high-performance miniaturized printed devices and EMI shields is feasible with our designed inks. All in all, proper rheological properties lead to high shape fidelity, high-resolution micro-thickness, and high-aspect-ratio 3D printing of deposited filaments, as shown in Fig. 1e (one layer), Fig. 1f (25 layers), and ESI Videos 2 and 3† for DMSO-doped PEDOT:PSS. In addition to shape fidelity, PEDOT:PSS inks showed printability on various rigid (glass) and flexible (polystyrene, cellulose acetate, and polyethylene terephthalate) substrates, as depicted in Fig. 1g and ESI Video 4,† which further expands the horizon of their application.

One of the most outstanding properties of PEDOT:PSS inks is the capability to manufacture flexible self-supporting geometries. As depicted in Fig. 2a and ESI Video 5,† a self-standing printed DMSO-doped 6 wt% PEDOT:PSS ink was achieved by printing the ink on spin-coated polydimethylsiloxane (PDMS) substrates, followed by dry-annealing (evaporating solvent and co-solvent at elevated temperatures) and then peeling off from the substrate. The thickness of the obtained structures is adjustable by defining the number of deposited layers. The electrical conductivity of the self-standing structures can be tuned using both co-solvent doping and/or solvent post-treatment approaches. Offering high flexibility, distinctive electrical conductivity, and visual transparency, free-standing patterned structures of solvent-treated PEDOT:PSS are versatile candidates for compact, flexible organic electronics, specifically EMI shields (refer to ESI Video 6†). However, as depicted in Fig. S6,† the addition of DMSO co-solvent to PEDOT:PSS led to a decrease in the elongations at break and Young's modulus of the prepared laminated films.

Common processing techniques are unable to manufacture patterned structures on sharp and uneven substrates as well as on the edges. Direct ink writing assists with fabricating patterned self-standing PEDOT:PSS EMI shields and structures, which can be transferred on unusual sharp, curved, and uneven complex edges/substrates using a wet-transfer technique (Fig. 2b). Lu *et al.*[44] showed that the partial removal of PSS due to co-solvent doping resulted in the formation of long-term (3 months) stable PEDOT:PSS hydrogels. Taking advantage of this outstanding attribute, the printed DMSO-doped PEDOT:PSS self-standing structures dipped in DI water showed high flexibility and stability (see ESI Video 7†), making them suitable to be easily transferred onto a substrate, *e.g.*, glass substrate, *via* a wet-transfer technique. The advantage of DIW and wet-transferring is that it overrides geometry limitations and provides highly conductive geometrically friendly structures, *i.e.*, it can be transferred onto geometries with any complex shape.

Additionally, ultra-lightweight aerogels (with a density of 0.1915–0.3871 g cm^{-3}) of 3D-printed DMSO-doped 6 wt% PEDOT:PSS with a high thickness were obtained using a freeze-drying technique, as depicted in Fig. 2c. Due to the low solid content of the prepared inks, the ultra-lightweight large-sized structure hovers over the delicate hairs of a cactus. Highly electrically conductive aerogels are high-performance candidates for lightweight EMI shields. As aforementioned, due to the appropriate rheological properties of the prepared inks, high-resolution micro/macro-scale 3D-printed aerogels with various infill patterns can be obtained. Fig. 2d shows a high-resolution and uniform microscopic image of a 3D-printed geometry with a triangle infill pattern for the DMSO-doped 6 wt% PEDOT:PSS ink. These printed structures were easily turned into aerogels without observable deformation or shrinkage, as demonstrated in SEM images (Fig. 2e and f). Red

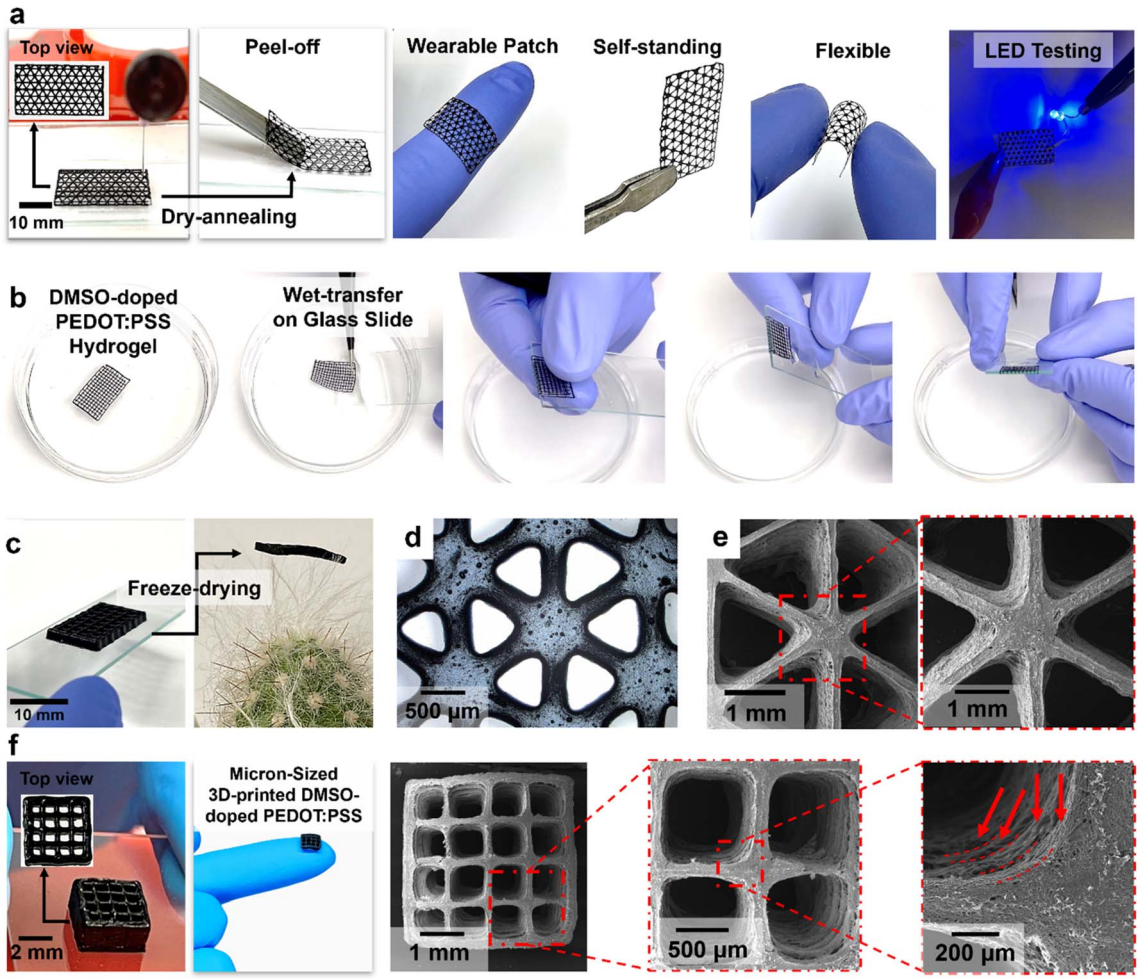

Fig. 2 Digital images of a flexible free-standing 3D-printed triangle-patterned structure on a PDMS substrate (a), digital images of the wet-transferring of free-standing hydrogels on the edge of a glass slide (b), digital images of an ultra-lightweight freeze-dried micro-scale 3D-printed geometry hovering over delicate cactus hair (c), microscopic image of a triangle-patterned structure (d), SEM micrographs of a freeze-dried triangle-infilled 3D-printed structure (e), and digital images and SEM micrographs of an as-printed and freeze-dried grid-infilled 3D-printed structure (f). All the printed structures are based on 6 wt% PEDOT:PSS doped with water : DMSO 93 : 7 vol/vol ink.

arrows in the magnified SEM images in Fig. 2f show orderly and high-resolution 3D-printed geometry that maintained its shape and structure after ink deposition. This confirms the capability of PEDOT:PSS inks for manufacturing reliable and uniform 3D architectures with different infill patterns (triangle and grid).

3.2. Topography

High zero-shear viscosity (viscosity at very low shear rates) and high storage modulus of the PEDOT:PSS inks allow for reliable and reproducible high-resolution printing of micro- and macro-scale printed electronics and EMI shields. The 3D-printed micrometer-thick lines of the PEDOT:PSS inks indicate a high-resolution DIW for architectures featuring various infill patterns and densities (Fig. 3). The digital images of the dry-annealed single-layer 3D-printed lines and various infill patterns of the DMSO-doped PEDOT:PSS ink is depicted in Fig. 3a and ESI Videos 8–10.† These results reveal high-resolution and high-quality printing. The achieved 2D and 3D topographical results from the laser microscope analysis (Fig. 3b) confirmed the uniform width and thickness of the printed lines. The line and surface roughness profiles of the printed lines of the printed ink are presented in Fig. S7,† depicting a uniform printed line profile with low surface roughness.

As illustrated in Fig. 3c–f, the micrometer-thick printed lines of the DMSO-doped PEDOT:PSS ink were achieved with an average width and thickness of 306.9 μm and 14.9 μm, respectively. A narrow distribution with less than 20% variation from the average values was achieved for both width and thickness using a printing nozzle with a 280 μm inner diameter. The deviation of the line average width (306.9 μm) from the inner diameter of the printing nozzle (280 μm) is negligible (~10%). According to the literature, the best-reported variation of the line's average width from the inner diameter of the printing nozzles was in the range of 20–120% for inks based on PEDOT:PSS containing 2D MXene nanosheets.[45–47] The resolution (minimum printed line width) achieved for different 3D printing techniques is summarized in Table S1.†

The printed line width and thickness can be adjusted by adjusting the rheological properties of the ink (concertation of PEDOT:PSS and the type of co-solvents) and printing parameters (*e.g.*, the injection speed, layer thickness, and inner diameter of the printing nozzle). The small line width deviation from the inner diameter of the printing nozzle facilitates the printing process for large-scale production of high-resolution printed electronics and EMI shields with accurate and reproducible homogeneity.

The obtained topographical results for the printed lines and geometries of the 6 wt% pristine PEDOT:PSS ink (Fig. 3c, e and S8†) indicate less than 25% line width variation from the average value (343.7 μm) and line thickness variation of less than 25% from the average value (13.92 μm). The larger average line width and smaller average thickness are due to the inferior rheological properties of pristine PEDOT:PSS ink (refer to Fig. 1) compared to co-solvent-doped PEDOT:PSS inks. The topographical findings for EG-doped PEDOT:PSS ink (Fig. 3c, e and S9†) showed a line width variation of less than 25% from the average width value (322.5 μm) and a line thickness variation of less than 15% from the average value (14.89 μm). The same examinations revealed that the printed lines of DMF-doped PEDOT:PSS inks displayed the smallest line width average (295.6 μm) with a line width variation of less than 15% and the smallest line average thickness (13.87 μm) with a line thickness variation of less than 20% (Fig. 3c, e and S10†). According to rheological data (see Fig. 1), the DMF-doped PEDOT:PSS inks exhibited the highest shear viscosity and viscoelastic moduli compared to the other inks, offering lower flowability and lower spreading after printing. Therefore, DMF-doped inks with slightly improved rheological properties displayed less width and thickness deviation from the average values. However, higher shear viscosity and yield stress demand higher working pressures.

Overall, by dry annealing at a high temperature (140 °C) right after printing, the evaporation of the solvent accelerates solidification, resulting in uniformly printed lines with minimal spreading. The high-temperature dry-annealing process reduces the activation energy of the PSS's partial phase separation and aids in the molecular penetration of PEDOT-rich grains.[48,49] Solvent and thermal treatments together enhance the electrical conductivity of the resulting inks as well as guarantee high-resolution printed structures, therefore boosting the final EMI shields' performance. These findings manifest the importance of ink formulation and confirm the reliability of the direct ink writing technique for manufacturing micro-scale printed electronics and EMI shields, provided that inks with proper rheological properties are designed.

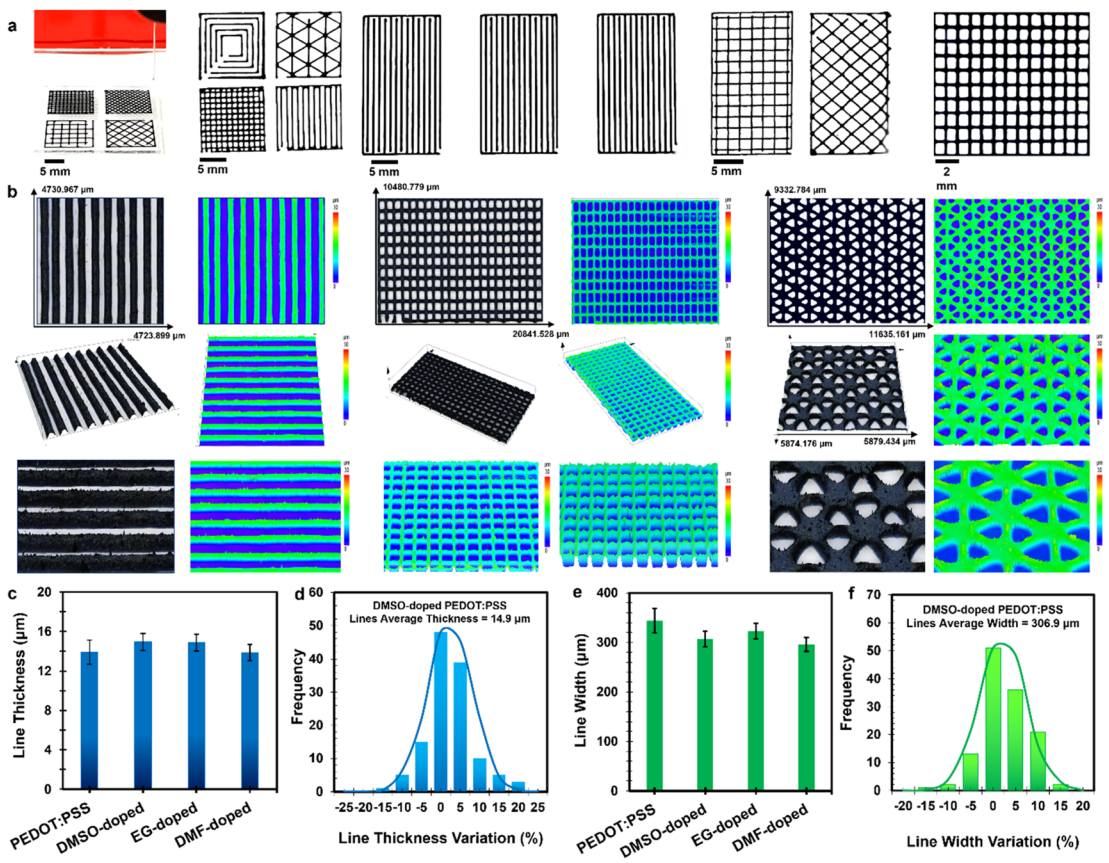

Fig. 3 Digital images of various printed patterned (a), topographical micrographs of the printed line-, grid-, and triangle-patterned (b) of DMSO-doped PEDOT:PSS ink. The average line thickness of different PEDOT:PSS-based inks (c), line thickness variation for DMSO-doped PEDOT:PSS (d), average line width variation for various PEDOT:PSS-based inks (e), and line width variation of the DMSO-doped PEDOT:PSS ink (f). All the printed structures are based on 6 wt% PEDOT:PSS doped with water : DMSO 93 : 7 vol/vol ink.

3.3. Electrical conductivity measurements

By increasing the concentration of co-solvents, the electrical conductivity rose to maximum values and then declined (Fig. 4a). The electrical conductivity increased from ~0.6 S cm^{-1} for pristine PEDOT:PSS to maximum values of 858.1 ± 60.8, 625.31 ± 39.98, and 492.81 ± 42 S cm^{-1} for the DMSO-doped, EG-doped, and DMF-doped PEDOT:PSS inks, respectively. Additionally, the solvent post-treatment of the printed pristine PEDOT:PSS films with various high boiling and low boiling (methanol and ethanol) point solvents showed similar enhancement trends for electrical conductivity. The highest electrical conductivity of 967 ± 97 S cm^{-1} was obtained for DMSO post-treated PEDOT:PSS ink compared to those for EG (801.76 ± 86 S cm^{-1}), DMF (828.63 ± 75.44 S cm^{-1}), methanol (813.78 ± 59 S cm^{-1}), and ethanol (444.96 ± 98 S cm^{-1}) post-treated PEDOT:PSS ones (Fig. 4d). The reported electrical conductivities of PEDOT:PSS films treated with various co-solvents and different preparation approaches are provided in Table S2.†

Electrical conductivity increased by more than three orders of magnitude after co-solvent doping and solvent post-treatment processes, followed by dry annealing. The enhancement in electrical conductivity after co-solvent doping lies behind the alteration in the structure of PEDOT:PSS due to the partial removal of PSS-rich grains surrounding the PEDOT-rich cores of the PEDOT:PSS gel particles. The weight ratio of PSS to PEDOT is usually 2.5 : 1 and a portion of the PSS chains is undoped with PEDOT, known as free PSS chains in the system. The presence of free PSS chains impedes electrical conductivity by forming non-conductive boundaries.[50] A smaller gel particle size results in a greater number of gel particle boundaries in dry conditions, blocking electron transfer between conductive PEDOT segments. Hence, the larger the gel particles, the fewer the boundaries, which gives rise to higher electrical conductivity.[11] The addition of co-solvents leads to the appearance of

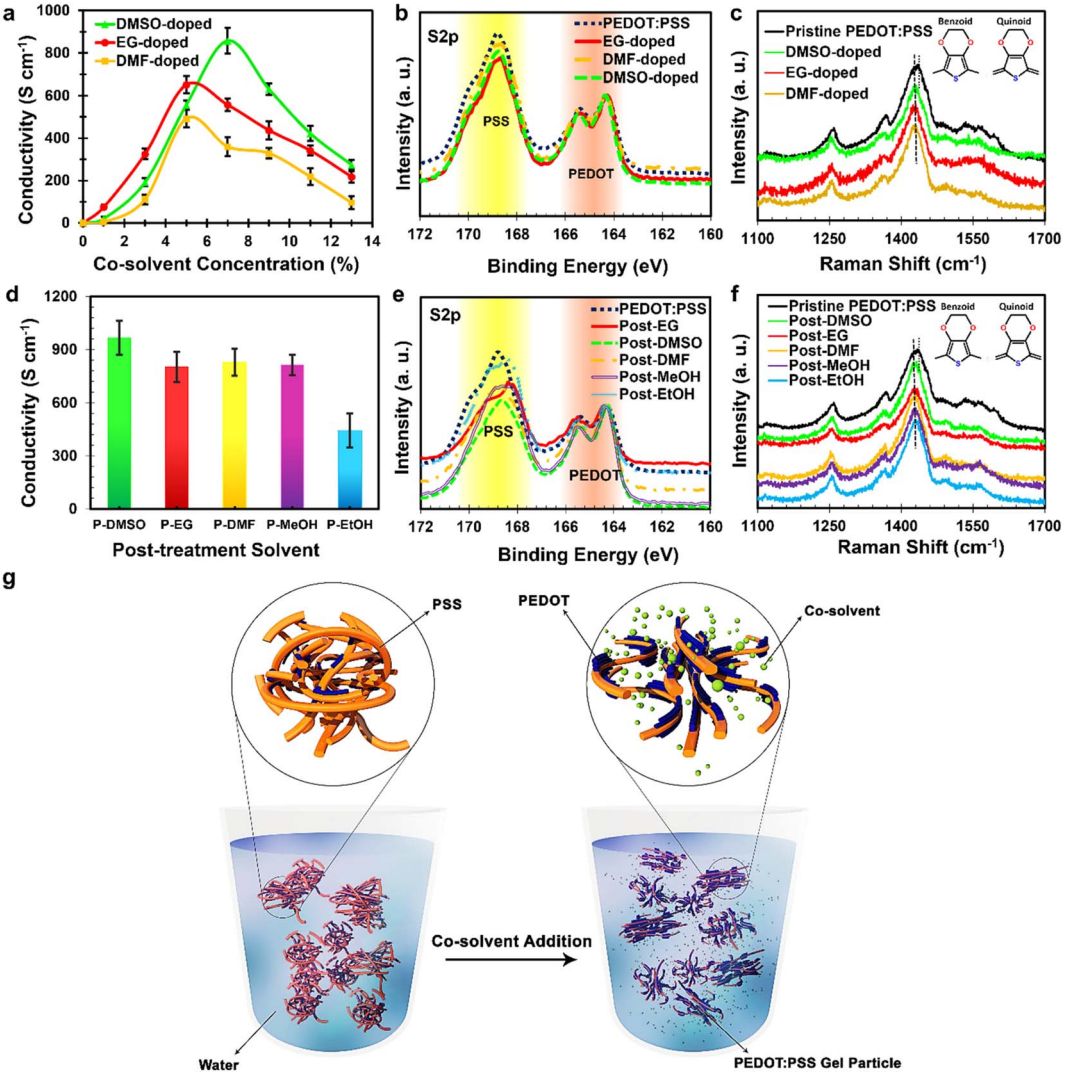

Fig. 4 Electrical conductivity (a), narrow-scan XPS spectra of the S2p signal (b), and Raman shifts (c) of co-solvent-doped printed PEDOT:PSS. Electrical conductivity (d), narrow-scan XPS spectra of the S2p signal (e), and Raman shifts (f) of solvent post-treated printed pristine PEDOT:PSS. Schematic illustration of PEDOT:PSS gel particles' structural changes after the co-solvent doping process (g).

strong electrostatic interactions between co-solvent molecules and PSS chains. At higher concentrations of co-solvent, the electrical conductivity declined, which could be attributed to the formation of PEDOT:PSS aggregations in the presence of excessive amounts of co-solvents.[51]

Additionally, the screening effect assists in distancing the PEDOT chain from PSS. Consequently, the partial PSS removal phenomenon occurs due to the high hydrophilicity of PSS. As shown in the narrow-scan XPS graphs (Fig. 4b and e), values of the PEDOT/PSS ratio were increased by adding co-solvents. The peak area for PEDOT and PSS can be used to estimate PSS removal from the system on the surface of the samples.[52,53] The calculated surface areas under the characteristic peaks of PEDOT (~165 eV) and PSS (~169 eV) in the achieved XPS spectra of co-solvent doped and solvent post-treated PEDOT:PSS inks proved that the presence of co-solvents increases the ratio of PEDOT/PSS (see Fig. S11†). It means that undoped PSS chains have been removed from the PEDOT:PSS gel particles to some extent. The higher PSS removal results in higher electrical conductivity because the pathways for transferring charge carriers increase.

In addition to the PSS-removal due to the incorporation of co-solvents/solvent post-treatment, the conformational transformation from a coiled structure of PEDOT to an extended structure leads to improved charge transport among PEDOT chains.[54] As demonstrated in Fig. 4c and f, the Raman shifts between the 1400 and 1500 cm^{-1} range are assigned to the stretching vibration of $C_\alpha = C_\beta$ on the fifth-member ring of PEDOT, exhibiting a red shift from 1437 cm^{-1} to lower values after co-solvent doping and solvent post-treatment. This Raman shift represents a structural resonant change in PEDOT chains from a benzoid structure to a quinoid one. This indicates that the former conformation of PSS chains is altered from a coil conformation to a linear or extended structure, which is desirable for improving electrical conductivity.[55]

Furthermore, XRD plots (Fig. S12†) revealed that the small shifting in the characteristic peaks at $2\theta = 5°$ to lower values represents an increase in the distance of the in-plane PSS and PEDOT chains (lamella stacking distance).[50,56] The slight slide of the peaks at $2\theta = 26°$ to higher values, due to co-solvent doping and solvent post-treatment, implies the reduction of the π–π stacking distance of PEDOT aromatic groups. Fig. S12† shows that the presence of co-solvents intensifies the sharpness of the characteristic peaks at $2\theta = 26°$, which is due to a decrease in the π–π stacking distance and, thus, an increase in the degree of molecular packing.[50] These structural changes in PEDOT:PSS on account of the incorporation of co-solvents indicate that the PEDOT π–π interchain couplings are intensified. Therefore, the π–π interchain charge transfer pathways were improved by increasing the π-electronic overlaps.[57] Structural changes in the PEDOT:PSS networks after co-solvent doping are schematically illustrated in Fig. 4g.

3.4. EMI shielding measurements

Inks with high electrical conductivity can be used to fabricate flexible, lightweight, and highly reproducible printed EMI shields with arbitrary geometries and sizes. The primary EMI shielding mechanism of highly conductive materials is the reflection of the incident wave, due to the impedance mismatch between free space and the shielding material.[58,59] For instance, in metallic EMI shields, the low impedance gives rise to a high ratio of reflection, which causes secondary EM wave (EMW) pollution. However, intrinsically conductive polymers have shown enhanced performance in absorbing the incident wave through the interaction of the EMW radiation with charge carriers, which induces polarization, Ohmic loss, scattering, and multiple internal reflections (in multiple-phase or porous EMI shields).[60,61]

Various inherent properties of the shield's constituents such as electrical conductivity, and geometrical features of the shield, *e.g.*, thickness, structure, and density, affect the total shielding effectiveness (SE_{Total}) in a specific frequency range of the incident EMW. As shown in Fig. 5a, different patterns, including laminated compact layers (100% infill density, labeled as Full), grid-infilled structures (with 1 and 2 mm line spacing, namely G1 and G2, respectively), and different numbers of deposited layers were 3D printed to correlate the macro-scale design of the shields to their shielding performance. By increasing the number of printed layers of the dry-annealed (DA) pristine PEDOT:PSS EMI shields with 100% infill density (Full) from one layer (11.66 μm) to ten layers (273.54 μm), the SE_{Total} increased from 16.61 dB to 28.35 dB (Fig. 5b) within the X-band (8.2–12.4 GHz). Expectedly, the grid-infilled printed EMI shields featured a lower SE_{Total} compared to the compact laminated films, which is a direct consequence of the reduced effective surface area. However, by increasing the number of deposited layers, the EMI SE of the grid-infilled structures increased dramatically. Findings revealed that the printed grid-infilled EMI shields of pristine PEDOT:PSS inks with at least five printed layers exhibited a SE_{Total} greater than 20 dB, which is suitable for a wide range of industry applications. A SE_{Total} of 20 dB can be translated to the shielding of 99% of the incident waves, and a SE_{Total} of 30 dB blocks 99.9% of the incident waves.

With advancements in technology, the demands for advanced high-performance EMI shields are increasing. The electrical conductivity of the shield affects the EMI SE_{Total} directly. Co-solvent doping and solvent post-treatment enhance the electrical conductivity of the prepared inks (refer to Fig. 4), and as a result of that, the EMI SE increases remarkably. Among the used co-solvents and solvent post-treatments, DMSO indicated the greatest influence on electrical conductivity. Solvent doping is of more importance due to the fewer processing steps and facile ink preparation; therefore, the EMI shielding performance of the prepared DMSO-doped PEDOT:PSS shields (858.1 ± 60.8 S cm^{-1}) was investigated. As shown in Fig. 5c, for the dry-annealed printed 100% infill density DMSO-doped PEDOT:PSS shields, the SE_{Total} reached 22.78 dB (1-layer, 9.4 μm), 27.49 dB (2-layer, 27.1 μm), 31.84 dB (5-layer, 43.3 μm), and 39.36 dB (10-layer, 196.7 μm). Interestingly, DIW enables the manufacturing of visually transparent patterned EMI shields with competitive performance compared to compact laminated structures (see Fig. S13†).

As indicated in Fig. 5c and Table 1, the dry-annealed printed grid-infilled DMSO-doped PEDOT:PSS shields with 1 mm line

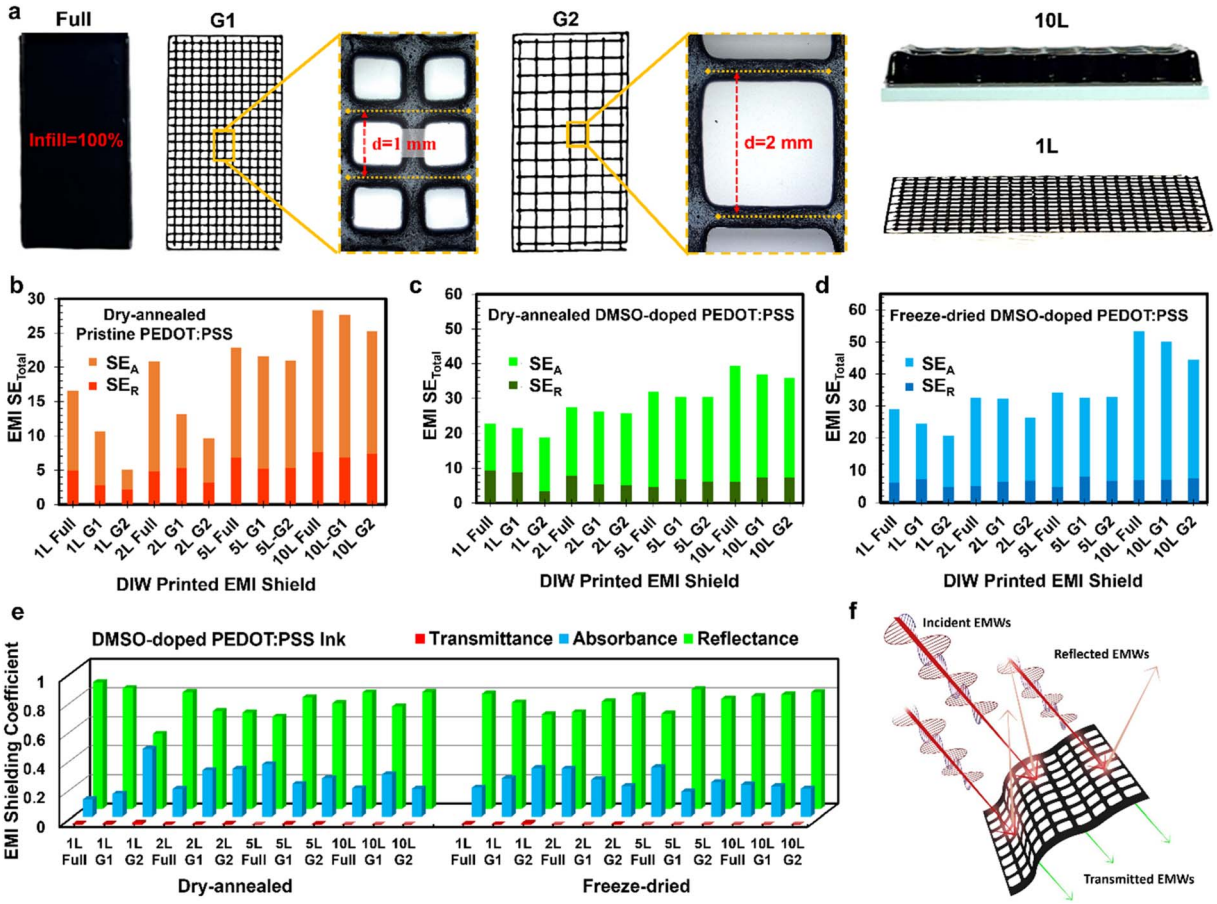

Fig. 5 Digital and microscopic images of the printed structures with different infill patterns and the number of printed layers (a). Total EMI SE of the printed pristine (b), dry-annealed DMSO-doped (c), and freeze-dried DMSO-doped (d) PEDOT:PSS structures. EMI shielding coefficients for DMSO-doped PEDOT:PSS structures (e). Schematic illustration of the EMI shielding mechanism of a grid-infilled printed structure (f). 1L and 10L represent 1 printed layer and 10 printed layers, respectively.

spacing (G1) show SE_{Total} of 23.50 dB (1-layer, 8 μm thickness), 26.14 dB (2-layer, 14.9 μm thickness), 30.55 (5-layer, 33.1 μm thickness), and 36.91 dB (10-layer, 184.2 μm thickness). By fabricating the grid-patterned structures, the empty spaces (openings) in the EMI shield give rise to the impedance mismatch between the free space and the shield. This leads to high EMI SE values despite the use of less material.

Additionally, the drying technique affects the final properties of the printed DMSO-doped PEDOT:PSS EMI shields. As illustrated in Fig. 5d and Table 1, employing a freeze-drying technique to fabricate EMI shields improves the EMI SE. This technique allowed the printed shields to maintain their micro- and macro-scale structures with higher thicknesses. Due to the increase in thickness as well as the increased micro-scale porosity of the freeze-dried samples, the incident electromagnetic waves are dissipated at higher rates due to the change in shielding mechanisms and improved multiple internal reflections.[62,63] According to Fig. S14,† freeze-drying samples showed increments of 19.55%, 20.18%, and 11.00% in EMI SE values for full, G1 grid-infilled, and G2 grid-infilled structures compared to dry-annealed samples. Fig. S15–S17† present the EMI SE reflection (SE_R), SE absorption (SE_A), and SE total (SE_{Total}) of the 3D-printed pristine PEDOT:PSS, dry-annealed DMSO-doped, and freeze-dried DMSO-doped PEDOT:PSS inks over the X-band range. It is clear that co-solvent doping increased the shielding performance throughout the entire frequency range, and patterning the EMI shields improved the absorption and reduced the reflection of the incident electromagnetic waves.

Since the thickness of different printed samples varies, the specific shielding effectiveness (SSE) is defined as the normalized SE_{Total} over the thickness of the shield (SE_{Total}/t) to present a better comparison. As listed in Table 1, printed shields with only one printed layer (1L) possess significant SSE values of 24 126.37, 27 040.09, and 23 729.66 dB cm^{-1} for Full, G1, and G2 dry-annealed DMSO-doped PEDOT:PSS structures, respectively. The SSE values decreased to 10 127.20, 17 497.59, and 17 200.11 dB cm^{-1} for 2-layered 100% infill, G1, and G2 EMI shields. The freeze-dried EMI shields have lower SSE values than the dry-annealed samples due to their higher thickness. Due to the structural differences between the dry-annealed and freeze-dried structures, normalizing SSE by the density of the printed EMI shields (absolute SE or SSE/d) provides a lucid comparison. Accordingly, the dry-annealed EMI shields with the

Table 1 EMI shield parameters of printed DMSO-doped PEDOT:PSS structures

	EMI shield	SE_R	SE_A	SE_{Total}	Thickness (mm)	SSE (dB cm^{-1})	SSE/d (dB cm^2 g^{-1})
Dry-annealed shields	1L Full	9.41	13.37	22.78	0.0094	24 126.37	69 251.05
	1L G1	8.94	12.56	21.50	0.0080	27 040.09	209 558.95
	1L G2	3.32	15.55	18.87	0.0080	23 729.66	306 505.52
	2L Full	7.91	19.58	27.49	0.0271	10 127.20	27 587.05
	2L G1	5.34	20.80	26.14	0.0149	17 497.59	126 564.86
	2L G2	5.08	20.61	25.70	0.0149	17 200.11	213 279.60
	5L Full	4.70	27.14	31.84	0.0433	7360.58	19 239.11
	5L G1	6.89	23.66	30.55	0.0331	9226.88	64 356.92
	5L G2	6.18	24.36	30.54	0.0331	9223.26	111 984.78
	10L Full	6.04	33.32	39.36	0.1967	2000.77	4876.05
	10L G1	7.37	29.54	36.91	0.1842	2003.77	13 458.56
	10L G2	7.40	28.59	35.99	0.1842	1953.68	23 216.06
Freeze-dried shields	1L Full	6.07	22.87	28.95	0.0167	17 343.08	90 564.40
	1L G1	7.34	17.14	24.48	0.0113	21 701.59	339 972.76
	1L G2	4.81	16.01	20.81	0.0113	18 451.18	481 754.05
	2L Full	5.07	27.49	32.57	0.0453	7184.67	36 782.22
	2L G1	6.37	25.93	32.31	0.0331	9754.46	142 623.97
	2L G2	6.88	19.49	26.38	0.0331	7963.86	199 616.42
	5L Full	4.95	29.39	34.34	0.3908	878.68	4411.93
	5L G1	8.14	24.40	32.53	0.3523	923.39	13 019.08
	5L G2	6.68	26.23	32.90	0.3523	933.91	22 921.02
	10L Full	6.89	46.40	53.30	0.6128	869.76	4284.72
	10L G1	7.11	43.05	50.16	0.5014	1000.35	13 581.82
	10L G2	7.45	36.92	44.37	0.5014	884.97	21 257.80

lowest printed layers (1L) maintain the highest values among the absolute SE values. Using DIW to print patterned EMI shields compensates for the impedance mismatch between free space and the EMI shields and reduces the required material for fabricating the shield. Therefore, engineering the structure of EMI shields leads to lower apparent density values and, thus, higher absolute SE values.

As listed in Table 1, 1-layered patterned DMSO-doped G1 and G2 EMI shields showed extraordinary absolute SE values of 209 558.95 and 306 505.52 dB cm^2 g^{-1}, respectively, compared to 1-layered full film (69 251.05 dB cm^2 g^{-1}). For EMI shields with 2 printed layers, the absolute SE values were 27 587.05, 126 564.86, and 213 279.60 dB cm^2 g^{-1} for Full, G1, and G2 samples, respectively. These outstanding achieved absolute SE values for different printed samples are comparable to previous works in the literature in which high levels of conductivity and EMI SSE were achieved using nanocomposites of PEDOT:PSS and different conductive nanofillers such as graphene,[64,65] MXenes,[45,66–68] and Ag NWs[69] (see Table S3†).

The freeze-dried 1-layered EMI shields showed remarkable absolute SE values for Full (90 564.40 dB cm^2 g^{-1}), G1 (339 972.76 dB cm^2 g^{-1}), and G2 (481 754.05 dB cm^2 g^{-1}). EMI shielding results showed that by increasing the number of the printed layers, the absolute SE decreased. For 10-layered printed EMI shields, the absolute SE values were 4284.72, 13 581.82, and 21 257.80 dB cm^2 g^{-1} for Full, G1, and G2 samples, respectively. These results are superior to those of the reported EMI shields in the literature (see Table S3†). All in all, the manufacturing technique (DIW) and drying method (freeze-drying) allow for controlling the macro- and micro-scale structures, respectively, of the manufactured high-performance lightweight EMI shields.

Other than the total SE, the shielding mechanism can be interpreted using EMI shielding coefficients. Interestingly, as shown in Fig. 5e, the reflection coefficient values decreased by decreasing the printed EMI shields' infill density. This indicates that by controlling the macro-scale design of the manufactured EMI shields, the mechanism of EMI shielding switches from reflection to Absorption. The printing of customized patterned structures not only uses less material but also improves the absorption mechanism of the engineered shields by changing the mechanism of shielding (see Fig. 5f).

4. Conclusions

High-performance engineered flexible EMI shields were manufactured using a DIW technique by formulating 3D printable highly electrically conductive PEDOT:PSS-based inks. EMI shielding characterizations indicated that by engineering the micro- and macro-scale design of the printed shields, the mechanism of shielding shifts from reflection to absorption. The highest EMI SE of 39.36 dB for dry-annealed and 50.16 dB for freeze-dried were achieved for 10 layers of the printed DMSO-doped PEDOT:PSS grid-infilled patterns. The electrical conductivity was enhanced by three orders of magnitude from ~0.6 S cm^{-1} for pristine PEDOT:PSS to 858.1 ± 60.8, 625.31 ± 39.98, and 492.81 ± 42 S cm^{-1} for the DMSO-doped, EG-doped, and DMF-doped PEDOT:PSS inks, respectively. The rheological properties of the PEDOT:PSS inks were fine-tuned by varying polymer concentrations and changing the type of co-solvent. The results indicated that the 6 wt% of pristine PEDOT:PSS inks feature proper viscoelastic properties, which were

improved by the addition of co-solvents, rendering them suitable for additive manufacturing of advanced flexible self-standing patterned EMI shields and printed electronics. Topographical analyses confirmed the high resolution of the printed structures. Pristine and EG-doped PEDOT:PSS inks showed lower printing resolution (higher spreading after printing) due to lower viscoelastic properties. However, DMSO- and DMF-doped PEDOT:PSS inks exhibited improved topographical profiles. The ink with the highest electrical conductivity (6 wt% PEDOT:PSS doped with water : DMSO 93 : 7 vol/vol) showed an average line width of 306.9 μm, an average line thickness of 14.9 μm, a line width/thickness variation of less than 20% from the average values, and line width with a 10% deviation from the inner diameter (280 μm) of the printing nozzle. This approves the reliability and reproducibility of the inks for the fabrication of pattern-infilled structures *via* the DIW technique. Electrical conductivity measurements showed that solvent post-treatment can be as effective as solvent doping. The maximum electrical conductivity of 967 ± 97 S cm^{-1} was obtained for the DMSO post-treated pristine PEDOT:PSS film compared to those for EG (801.76 ± 86), DMF (828.63 ± 75.44), methanol (813.78 ± 59), and ethanol (444.96 ± 98) post-treated PEDOT:PSS ones. The experimental results demonstrated the partial removal of non-conductive PSS from the conductive PEDOT cores, as well as PEDOT structural transformations, thereby leading to an enhancement in the electrical conductivity of the printed structures.

Author contributions

Saeed Ghaderi: conceptualization, data curation, formal analysis, investigation, methodology, project administration, validation, visualization, writing–original draft, writing–review & editing. Hadi Hosseini: conceptualization, data curation, formal analysis, methodology, validation, visualization, writing–review & editing. Seyyed Arash Haddadi: validation, writing–review & editing. Milad Kamkar: conceptualization, methodology, validation, writing–review & editing. Mohammad Arjmand: conceptualization, data curation, funding acquisition, project administration, resources, supervision, validation, writing–review & editing.

Conflicts of interest

The authors declare no conflict of interest.

Note added after first publication

This article replaces the version published on 8 June 2023, which contained DFT simulation work which has now been removed.

Acknowledgements

The authors acknowledge the Syilx Okanagan Nation for the use of their traditional, ancestral, and unceded territory, the land on which the research was conducted. Dr Arjmand acknowledges the support of the Natural Sciences and Engineering Research Council of Canada (NSERC) [NSERC Alliance Grant – funding reference number: ALLRP 555586-20 and Discovery Grant – funding reference number: RGPIN-2020-03914]. Dr Arjmand appreciates the financial support provided by the Canada Research Chairs Program (CRC-2018-00234).

References

1 L. V. Kayser and D. J. Lipomi, *Adv. Mater.*, 2019, **31**, 1806133.
2 Y. Yang, H. Deng and Q. Fu, *Mater. Chem. Front.*, 2020, **4**, 3130–3152.
3 L. Xiong, H. Jin, Y. Lu, X. Li, X. Ai, H. Yang and L. Huang, *Macromol. Mater. Eng.*, 2020, **305**, 2000327.
4 S. Khasim, A. Pasha, M. Lakshmi, P. Chellasamy, M. Kadarkarai, A. A. A. Darwish, T. A. Hamdalla, S. A. Al-Ghamdi and S. Alfadhli, *Opt. Mater.*, 2022, **125**, 112109.
5 Z. Fan and J. Ouyang, *Adv. Electron. Mater.*, 2019, **5**, 1800769.
6 L. Manjakkal, A. Pullanchiyodan, N. Yogeswaran, E. S. Hosseini and R. Dahiya, *Adv. Mater.*, 2020, **32**, 1907254.
7 L. Hu, J. Song, X. Yin, Z. Su and Z. Li, *Polymers*, 2020, **12**, 145.
8 E. Dauzon, Y. Lin, H. Faber, E. Yengel, X. Sallenave, C. Plesse, F. Goubard, A. Amassian and T. D. Anthopoulos, *Adv. Funct. Mater.*, 2020, **30**, 2001251.
9 E. Hosseini, M. Arjmand, U. Sundararaj and K. Karan, *ACS Appl. Mater. Interfaces*, 2020, **12**, 28596–28606.
10 Y. Xiao, Y. Xu, C. Qu, H. Liu, S. Zhang, F. Lin, W. Wu and G. Song, *Adv. Mater. Technol.*, 2022, **7**, 2100423.
11 I. F. Perepichka and D. F. Perepichka, *Handbook of Thiophene-Based Materials: Applications in Organic Electronics and Photonics*, 2 Volume Set, John Wiley & Sons, 2009.
12 L. Groenendaal, F. Jonas, D. Freitag, H. Pielartzik and J. R. Reynolds, *Adv. Mater.*, 2000, **12**, 481–494.
13 S. Ghosh and O. Inganäs, *J. Electrochem. Soc.*, 2000, **147**, 1872.
14 S. Kirchmeyer and K. Reuter, *J. Mater. Chem.*, 2005, **15**, 2077–2088.
15 S. T. Keene, W. Michaels, A. Melianas, T. J. Quill, E. J. Fuller, A. Giovannitti, I. McCulloch, A. A. Talin, C. J. Tassone and J. Qin, *J. Am. Chem. Soc.*, 2022, **144**(23), 10368–10376.
16 J. Ouyang, *Displays*, 2013, **34**, 423–436.
17 J. Zhou, D. H. Anjum, L. Chen, X. Xu, I. A. Ventura, L. Jiang and G. Lubineau, *J. Mater. Chem. C*, 2014, **2**, 9903–9910.
18 U. Lang, E. Müller, N. Naujoks and J. Dual, *Adv. Funct. Mater.*, 2009, **19**, 1215–1220.
19 T. Takano, H. Masunaga, A. Fujiwara, H. Okuzaki and T. Sasaki, *Macromolecules*, 2012, **45**, 3859–3865.
20 Q. Wei, M. Mukaida, Y. Naitoh and T. Ishida, *Adv. Mater.*, 2013, **25**, 2831–2836.
21 T.-R. Chou, S.-H. Chen, Y.-T. Chiang, Y.-T. Lin and C.-Y. Chao, *J. Mater. Chem. C*, 2015, **3**, 3760–3766.
22 Y. H. Kim, C. Sachse, M. L. Machala, C. May, L. Müller-Meskamp and K. Leo, *Adv. Funct. Mater.*, 2011, **21**, 1076–1081.

23 F. Wu, P. Li, K. Sun, Y. Zhou, W. Chen, J. Fu, M. Li, S. Lu, D. Wei and X. Tang, *Adv. Electron. Mater.*, 2017, **3**, 1700047.
24 H. Shi, C. Liu, Q. Jiang and J. Xu, *Adv. Electron. Mater.*, 2015, **1**, 1500017.
25 E. Yildirim, G. Wu, X. Yong, T. L. Tan, Q. Zhu, J. Xu, J. Ouyang, J.-S. Wang and S.-W. Yang, *J. Mater. Chem. C*, 2018, **6**, 5122–5131.
26 W.-H. Chen, L. Qiu, P. Zhang, P.-C. Jiang, P. Du, L. Song, J. Xiong and F. Ko, *J. Mater. Chem. C*, 2019, **7**, 10247–10256.
27 S. K. Sinha, Y. Noh, N. Reljin, G. M. Treich, S. Hajeb-Mohammadalipour, Y. Guo, K. H. Chon and G. A. Sotzing, *ACS Appl. Mater. Interfaces*, 2017, **9**, 37524–37528.
28 C. Zhu, A. Chortos, Y. Wang, R. Pfattner, T. Lei, A. C. Hinckley, I. Pochorovski, X. Yan, J. W.-F. To and J. Y. Oh, *Nat. Electron.*, 2018, **1**, 183–190.
29 H. Sirringhaus, T. Kawase, R. H. Friend, T. Shimoda, M. Inbasekaran, W. Wu and E. P. Woo, *Science*, 2000, **290**, 2123–2126.
30 Y. Wang, C. Zhu, R. Pfattner, H. Yan, L. Jin, S. Chen, F. Molina-Lopez, F. Lissel, J. Liu and N. I. Rabiah, *Sci. Adv.*, 2017, **3**, e1602076.
31 V. R. Feig, H. Tran, M. Lee, K. Liu, Z. Huang, L. Beker, D. G. Mackanic and Z. Bao, *Adv. Mater.*, 2019, **31**, 1902869.
32 K. Hong, Y. H. Kim, S. H. Kim, W. Xie, W. D. Xu, C. H. Kim and C. D. Frisbie, *Adv. Mater.*, 2014, **26**, 7032–7037.
33 H. Yuk, B. Lu, S. Lin, K. Qu, J. Xu, J. Luo and X. Zhao, *Nat. Commun.*, 2020, **11**, 1–8.
34 M. M. Ovhal, N. Kumar and J.-W. Kang, *Mol. Cryst. Liq. Cryst.*, 2020, **705**, 105–111.
35 S. Tagliaferri, A. Panagiotopoulos and C. Mattevi, *Mater. Adv.*, 2021, **2**, 540–563.
36 L. Li, J. Meng, X. Bao, Y. Huang, X.-P. Yan, H.-L. Qian, Ch. Zhang and T. Liu, *Adv. Energy Mater.*, 2023, **13**, 2203683.
37 J. A. Lewis, *Adv. Funct. Mater.*, 2006, **16**, 2193–2204.
38 S. Ghaderi, M. Kamkar, A. Ghaffarkhah, M. Amini, A. H. A. Hosein and M. Arjmand, in *2021 IEEE Sensors*, IEEE, 2021, pp. 1–4.
39 M. Amini, M. Kamkar, F. Ahmadijokani, S. Ghaderi, O. J. Rojas, H. Hosseini and M. Arjmand, *Biomacromolecules*, 2023, **24**(2), 775–788.
40 J. Liu, L. Mckeon, J. Garcia, S. Pinilla, S. Barwich, M. Möbius, P. Stamenov, J. N. Coleman and V. Nicolosi, *Adv. Mater.*, 2022, **34**, 2106253.
41 M. Saadi, A. Maguire, N. Pottackal, M. S. H. Thakur, M. M. Ikram, A. J. Hart, P. M. Ajayan and M. M. Rahman, *Adv. Mater.*, 2022, 2108855.
42 J. Liu, L. Mckeon, J. Garcia, S. Pinilla, S. Barwich, M. Möbius, P. Stamenov, J. N. Coleman and V. Nicolosi, *Adv. Mater.*, 2022, **34**, 2106253.
43 H. Yuk, B. Lu, S. Lin, K. Qu, J. Xu, J. Luo and X. Zhao, *Nat. Commun.*, 2020, **11**, 1–8.
44 B. Lu, H. Yuk, S. Lin, N. Jian, K. Qu, J. Xu and X. Zhao, *Nat. Commun.*, 2019, **10**, 1043.
45 A. Ghaffarkhah, M. Kamkar, Z. A. Dijvejin, H. Riazi, S. Ghaderi, K. Golovin, M. Soroush and M. Arjmand, *Carbon*, 2022, **191**, 277–289.
46 L. Yu, Z. Fan, Y. Shao, Z. Tian, J. Sun and Z. Liu, *Adv. Energy Mater.*, 2019, **9**, 1901839.
47 J. Orangi, F. Hamade, V. A. Davis and M. Beidaghi, *ACS Nano*, 2019, **14**, 640–650.
48 Y. Xia and J. Ouyang, *J. Mater. Chem.*, 2011, **21**, 4927–4936.
49 C. M. Palumbiny, F. Liu, T. P. Russell, A. Hexemer, C. Wang and P. Müller-Buschbaum, *Adv. Mater.*, 2015, **27**, 3391–3397.
50 N. Kim, B. H. Lee, D. Choi, G. Kim, H. Kim, J.-R. Kim, J. Lee, Y. H. Kahng and K. Lee, *Phys. Rev. Lett.*, 2012, **109**, 106405.
51 B. Lu, H. Yuk, S. Lin, N. Jian, K. Qu, J. Xu and X. Zhao, *Nat. Commun.*, 2019, **10**, 1043.
52 J. P. Thomas, L. Zhao, D. McGillivray and K. T. Leung, *J. Mater. Chem. A*, 2014, **2**, 2383–2389.
53 J. P. Thomas and K. T. Leung, *Adv. Funct. Mater.*, 2014, **24**, 4978–4985.
54 A. Corletto and J. G. Shapter, *J. Mater. Chem. C*, 2021, **9**, 14161–14174.
55 J. Ouyang, Q. Xu, C.-W. Chu, Y. Yang, G. Li and J. Shinar, *Polymer*, 2004, **45**, 8443–8450.
56 E. Hosseini, V. O. Kollath and K. Karan, *J. Mater. Chem. C*, 2020, **8**, 3982–3990.
57 H. C. F. Martens, H. B. Brom and R. Menon, *Phys. Rev. B: Condens. Matter Mater. Phys.*, 2001, **64**, 201102.
58 M. Kamkar, E. Erfanian, P. Bazazi, A. Ghaffarkhah, F. Sharif, G. Xie, A. Kannan, M. Arjmand, S. H. Hejazi and T. P. Russell, *Adv. Mater. Interfaces*, 2022, **9**, 2101659.
59 M. Amini, M. Kamkar, F. Rahmani, A. Ghaffarkhah, F. Ahmadijokani and M. Arjmand, *ACS Appl. Electron. Mater.*, 2021, **3**, 5514–5527.
60 S. Sankaran, K. Deshmukh, M. B. Ahamed and S. K. K. Pasha, *Composites, Part A*, 2018, **114**, 49–71.
61 C. M. Koo, P. Sambyal, A. Iqbal, F. Shahzad and J. Hong, *Two-Dimensional Materials for Electromagnetic Shielding*, John Wiley & Sons, 2021.
62 Z. Ma, H. Feng, Y. Feng, X. Ding, X. Wang, W. Wang, X. Zhang, S. Kong, X. Lan and Q. Li, *J. Mater. Chem. C*, 2022, **10**, 14169–14179.
63 Q. Li, L. Chen, J. Ding, J. Zhang, X. Li, K. Zheng, X. Zhang and X. Tian, *Carbon*, 2016, **104**, 90–105.
64 N. Agnihotri, K. Chakrabarti and A. De, *RSC Adv.*, 2015, **5**, 43765–43771.
65 Y. Wu, Z. Wang, X. Liu, X. Shen, Q. Zheng, Q. Xue and J.-K. Kim, *ACS Appl. Mater. Interfaces*, 2017, **9**, 9059–9069.
66 R. Liu, M. Miao, Y. Li, J. Zhang, S. Cao and X. Feng, *ACS Appl. Mater. Interfaces*, 2018, **10**, 44787–44795.
67 P. J. Bora, A. G. Anil, P. C. Ramamurthy and D. Q. Tan, *Mater. Adv.*, 2020, **1**, 177–183.
68 G.-Y. Yang, S.-Z. Wang, H.-T. Sun, X.-M. Yao, C.-B. Li, Y.-J. Li and J.-J. Jiang, *ACS Appl. Mater. Interfaces*, 2021, **13**, 57521–57531.
69 J. Yu, W. Gu, H. Zhao and G. Ji, *Sci. China Mater.*, 2021, **64**, 1723–1732.

